ACS APPLIED NANO MATERIALS

www.acsanm.org

Article

Effective Space Confinement by Inverse Miniemulsion for the Controlled Synthesis of Undoped and Eu^{3+}-Doped Calcium Molybdate Nanophosphors: A Systematic Comparison with Batch Synthesis

Chiara Mazzariol, Francesca Tajoli, Alexander E. Sedykh, Paolo Dolcet, Jan-Dierk Grunwaldt, Klaus Müller-Buschbaum,* and Silvia Gross*

Cite This: *ACS Appl. Nano Mater.* 2023, 6, 15510−15520

Read Online

ACCESS | Metrics & More | Article Recommendations | Supporting Information

ABSTRACT: The possibility to precisely control reaction outcomes for pursuing materials with well-defined features is a main endeavor in the development of inorganic materials. Confining reactions within a confined space, such as nanoreactors, is an extremely promising methodology which allows to ensure control over the final properties of the material. An effective room temperature inverse miniemulsion approach for the controlled synthesis of undoped and Eu^{3+}-doped calcium molybdate crystalline nanophosphors was developed. The advantages and the efficiency of confined space in terms of controlling nanoparticle features like size, shape, and functional properties are highlighted by systematically comparing miniemulsion products with calcium molybdate particles obtained without confinement from a typical batch synthesis. A relevant beneficial impact of space confinement by miniemulsion nanodroplets is observed on the control of size and shape of the final nanoparticles, resulting in 12 nm spherical nanoparticles with a narrow size distribution, as compared to the 58 nm irregularly shaped and aggregated particles from the batch approach (assessed by TEM analysis). Further considerable effects of the confined space for the miniemulsion samples are found on the doping effectiveness, leading to a more homogeneous distribution of the Eu^{3+} ions into the molybdate host matrix, without segregation (assessed by PXRD, XAS, and ICP-MS). These findings are finally related to the photoluminescence properties, which are evidenced to be closely dependent on the Eu^{3+} content for the miniemulsion samples, as an increase of the relative intensity of the direct *f*−*f* excitation and a shortening of the lifetime (from 0.901 ms for 1 at. % to 0.625 ms for 7 at. % samples) with increasing Eu^{3+} content are observed, whereas no relationship between these parameters and the Eu^{3+} content is evidenced for the batch samples. All these results are ascribed to the uniform and controlled crystallization occurring inside each miniemulsion nanodroplet, as opposed to the less controlled nucleation and growth for a classic nonconfined approach.

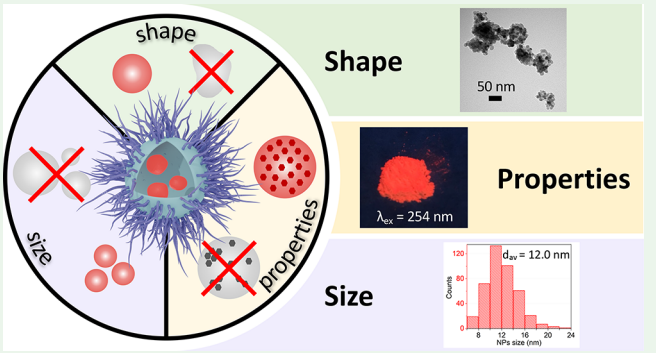

KEYWORDS: *confined space, lanthanides, luminescence, miniemulsion, nanophosphors, nanoreactors*

INTRODUCTION

The possibility to control the size, shape, and crystalline phase of inorganic nanomaterials is currently of great interest in modern inorganic material chemistry.[1] Synthesizing inorganic nanomaterials within the constrained environment of nanoreactors[2,3] is a viable and effective route to control these features, which all play a relevant role in determining material functional properties.[1] Confined space (CS) is currently defined as an enclosed volume, in the nm^3 range, with limited volume and accessibility,[2,4] e.g., meso-[5] or nanopores,[2,6] droplets or bubbles,[7,8] and supramolecular cages.[9] As far as the crystallization of inorganic nanostructures is concerned, it has been widely reported that the phase diagrams and phase transformation kinetics of matter in CS can deviate considerably from their behavior in bulk.[10−12]

Among different types of nanoreactors, miniemulsions (MEs) are heterophase systems characterized by droplets with a mean diameter ranging between 50 and 300 nm, which are stabilized toward both diffusion (Ostwald ripening)- and

Received: May 13, 2023
Accepted: July 31, 2023
Published: August 28, 2023

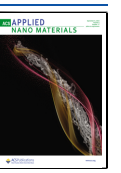

Scheme 1. (a) Schematic Representation of the Synthesis of Eu^{3+}-Doped Calcium Molybdate in Water-in-Oil ME by a Cohomogenization Approach (US = Application of Ultrasounds) and (b) Crystalline Structure of Calcium Molybdate (Spheres: Blue = Ca, Purple = Mo, and Red = O)

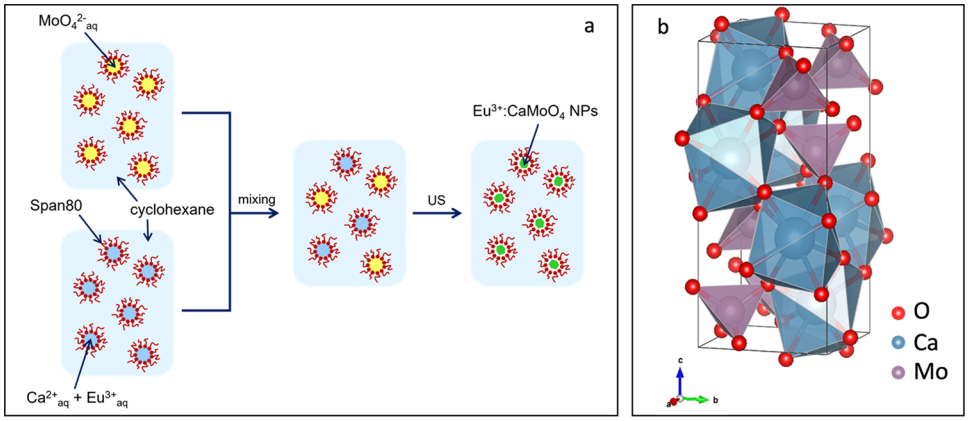

collision (coalescence)-induced degradation processes.[13,14] MEs are prepared by high-shear treatment (e.g., by high-power ultrasounds) of a mixture of two immiscible phases, a surfactant and an additive that is soluble only into the dispersed phase, i.e., the osmotic agent. The nanodroplets forming MEs are considered to be independent of each other, as there is no interdroplet reactant exchange and they are stabilized, among others, by the balance between the outward Laplace pressure and the inward osmotic pressure, thus maintaining their identity on the scale of days to months.[15] Thanks to these peculiar features of MEs, inorganic systems can be synthesized in a parallel fashion inside the constrained environment of inverse (i.e., water-in-oil) ME nanodroplets.[16] This synthetic approach ensures a uniform crystallization, leading to excellent control of the size and shape of the final nanoparticles (NPs), as well as prevents aggregation phenomena, as recently explored by our group for the synthesis of oxides, sulfides, and halogenides.[17−22] Although it is well known that the CS plays a crucial role in the outcomes of the syntheses that are performed within it, by affecting the chemical−physical properties of the precursor(s) and of the solvent molecules, and possibly promoting the crystallization of inorganic NPs at lower or even at room temperature, a deep understanding of its effect is still far from being complete, mostly due to the lack of mechanistic data. Moreover, thorough studies systematically comparing synthesis in CSs with syntheses performed in batch (without space confinement) are needed to rationalize how and to what extent constrained environments affect the crystallization of the target inorganic material. Recently, our group demonstrated that miniemulsion nanodroplets' spatial constraint can enable different crystallization pathways with respect to the classical ones,[22] and in this paper, we provide additional insights into ME CS as a successful unconventional approach to the controlled synthesis of functional inorganic materials.

In particular, we address for the first time the crystallization of the model system $CaMoO_4$ (CM) in the CS of inverse ME water-in-oil nanodroplets (Scheme 1a). Calcium molybdate occurs in nature as a mineral named powellite, and it belongs to the family of the scheelite-type systems AXO_4 (where A is a large cation, such as Ca^{2+}, Sr^{2+}, Ba^{2+}, or Mg^{2+} and $[XO_4]^{2-}$ is an anion with X = Mo or W). The crystalline structure of calcium molybdate (Scheme 1b) is a tetragonal body-centered scheelite-type structure, whose space group is $I4_1/a$ (n. 88) with a C_{4h}^6 point-group symmetry.[23] The structure is based on tetragonal MoO_4 units surrounded by eight CaO_8 polyhedra in a distorted pseudocubic configuration, in which each CaO_8 shares eight corners with eight adjacent MoO_4 tetrahedra.[24] Due to its intrinsic photoluminescence (PL) properties[24−26] and its chemical and thermal stability, the target system, calcium molybdate, is a promising photoluminescent material and an interesting versatile host matrix for the development of Ln-based phosphors (Ln = lanthanide ion).[27,28] In the crystalline structure of Ln-doped calcium molybdate, the dopant ions, e.g., Eu^{3+}, should replace the Ca^{2+} ions on their site (aliovalent substitution).[28] CM, notably if doped with rare earth ions,[27,28] is currently employed as a phosphor or laser material, in white-light emitting diodes, scintillators detectors, and upconversion devices[29] and for the enhanced latent fingerprint detection.[30]

In recent years, a variety of methods have been proposed for the synthesis of undoped and Eu^{3+}-doped CM, such as the hydrothermal process,[31,32] microwave-assisted synthesis,[33] pulsed laser ablation,[34] coprecipitation,[35,36] and microemulsion approach.[37,38] Generally, a variety of morphologies and sizes (nano- and microparticles), as well as a good shape control over the final particle aggregation into mesostructures, are reported. However, up to date, no studies of the synthesis of calcium molybdate in the CS of ME droplets, preventing the formation of aggregated microstructures, have been reported.

Herein, we focus on unveiling the advantages of the ME nanodroplet space confinement on the synthesis of calcium molybdate crystalline NPs, both undoped and doped with Eu^{3+} ions, leading to excellent control over the final features of the material, such as reduced particle size down to 10−15 nm, improved homogeneity of dopant distribution, and resulting PL properties. For this purpose, a systematic and comprehensive comparison of the ME synthesis outcomes with a batch approach, taken as a reference for a "macroreactor" synthetic strategy without any spatial constraint, is carried out. By systematically comparing the results obtained from the two synthetic approaches, we demonstrate that the space confinement provided by the ME nanodroplets plays a pivotal role in controlling the crystallite size, and size, size distribution, morphology, and aggregation state of the CM NPs, as evidenced by powder X-ray diffraction (PXRD), transmission electron microscopy (TEM), and Brunauer−Emmett−Teller (BET) analyses. In addition, the confined space is found to be

https://doi.org/10.1021/acsanm.3c02136
ACS Appl. Nano Mater. 2023, 6, 15510−15520

effective for pursuing a homogeneous distribution of the Eu^{3+} ions in the molybdate host matrix and for improving the functional PL properties of the final CM products, as confirmed by inductively coupled plasma-mass spectrometry (ICP-MS) and X-ray absorption spectroscopy (XAS) at the Eu L_3-edge and Mo K-edge, and optical investigations (PL and diffuse reflectance spectroscopy (DRS)).

EXPERIMENTAL SECTION

Chemicals. Calcium nitrate tetrahydrate $Ca(NO_3)_2{\cdot}4H_2O$ (Carlo Erba, 99%), sodium molybdate dihydrate $Na_2MoO_4{\cdot}2H_2O$ (Alfa Aesar, 98%), europium nitrate pentahydrate $Eu(NO_3)_3{\cdot}5H_2O$ (Sigma-Aldrich, 99.9%), cyclohexane (Sigma-Aldrich, ≥99%), Span 80 (Sigma-Aldrich) were used. All chemicals were used without further purification.

Inverse ME Synthesis. Calcium molybdate nanostructures were synthesized at room temperature (RT) through an inverse (water-in-oil) ME approach with a cohomogenization method (Scheme 1a). Two starting mixtures of the precursors, A and B, were prepared by mechanically stirring a mixture of a 0.2 M (1.2 mmol) aqueous solution of the precursor (either $Na_2MoO_4{\cdot}2H_2O$ or $Ca(NO_3)_2{\cdot}4H_2O$) and a solution of 1.5% w/w surfactant Span 80 in cyclohexane. The weight ratio between the aqueous (dispersed) and oil (continuous) phases was 1:3. Emulsions A and B were ultrasonicated at 280 W (0.9 s pulse) separately for 2 min, with a Sartorius Stedim LabsonicP tip sonicator, equipped with a titanium tip of 3 mm of diameter, resulting in white turbid inverse MEs A′ and B′. The droplet size of the inverse MEs A′ and B′, estimated by dynamic light scattering (DLS) analysis (Figure S1), are about 100 nm. Then, the inverse MEs A′ and B′ were mixed together and ultrasonicated again for 2 min (280 W, 0.9 s pulse), in order to promote the mixing of the reactants within the droplets, thus allowing the reaction to occur inside the droplets. The resulting suspension was left under mechanical stirring at RT for 24 h. The product was isolated and purified by centrifugation at 12000 rpm for 5 min with acetone and deionized water and dried under vacuum at RT for 3 h. The purity of the samples regarding the removal of the surfactant was investigated via ATR-FTIR (Supporting Information (SI) Section S2.2). Different concentrations of both the Ca^{2+} and MoO_4^{2-} aqueous precursor solutions were screened (0.15, 0.20, 0.25, 0.50, 1.0, 1.5, and 2.0 M), by maintaining the molar ratio between Ca^{2+} and MoO_4^{2-} as 1:1 mol.

Batch Synthesis (without Confinement). An aqueous 0.2 M $Ca(NO_3)_2{\cdot}4H_2O$ precursor solution (1.2 mmol) was added dropwise, under mechanical stirring at RT, to an aqueous 0.2 M $Na_2MoO_4{\cdot}2H_2O$ precursor solution (1.2 mmol). A white solid precipitated immediately, and the reaction mixture was left under mechanical stirring at RT for 24 h. The precipitate was purified by centrifugation at 12000 rpm for 5 min with deionized water and acetone and dried under vacuum at RT for 3 h. Different concentrations of both the Ca^{2+} and MoO_4^{2-} aqueous precursor solutions were screened (0.15, 0.20, 0.25, 0.50, 1.0, 1.5, and 2.0 M), by maintaining the molar ratio between Ca^{2+} and MoO_4^{2-} as 1:1 mol.

Eu^{3+}-Doped Calcium Molybdate Synthesis. $Eu(NO_3)_3{\cdot}5H_2O$ was used as the precursor for the dopant ions Eu^{3+}. The Eu^{3+} ions were added in a stoichiometric amount to the Ca^{2+} precursor solution. Therefore, the synthesis and purification of the products were performed with the same steps as for the inverse miniemulsion and the batch syntheses, as described above. The doping level (at. %) was calculated as the Eu/Mo molar ratio. The molar ratio between (Ca^{2+} + Eu^{3+}) and MoO_4^{2-} was always kept as 1:1 mol throughout all the syntheses of the doped samples. Different doping levels (1, 3, 5, and 7 at. %) were tested.

Characterization Techniques. A thorough description of all the analytical methods is reported in SI Section S1.3.

Powder X-ray Diffraction. PXRD measurements were conducted using a Bruker D8 Advance diffractometer, fitted with a LYNXEYE detector in 1D mode (Department of Chemical Sciences, University of Padova). Diffraction data were acquired by exposing powder samples to Cu-K$\alpha_{1,2}$ X-ray radiation. X-rays were generated from a Cu anode supplied with 40 kV and a current of 40 mA. The data were collected over the 10−80° 2θ range with a step size of 0.014° 2θ and a nominal time per step of 0.3 s. Fixed divergence slits of 0.50° were used together with Soller slits with an aperture of 2.5°. The experimental diffractograms were fitted by using the software Bruker DIFFRAC.TOPAS, to estimate crystallographic and microstructural information by using the whole powder pattern fitting (WPPF) method.[39,40]

Transmission Electron Microscopy. TEM images were acquired with an FEI Tecnai G2 microscope (Department of Biology, University of Padova), working at 100 kV, equipped with an Olympus Veleta camera and a TVIPS F114 camera. For the sample preparation, a suspension in ethanol of each sample under investigation was deposited on a carbon-coated copper grating.

N_2 Physisorption. The N_2 adsorption/desorption isotherms were recorded at 77 K by using a Quantachrome Autosorb AS-1C using AS1win software (Department of Inorganic and Analytical Chemistry, Justus Liebig University Giessen). Before the measurements, the samples were degassed at 120 °C for 19 h under vacuum, to ensure the complete removal of any previous adsorbate. For the isotherms, N_2 (Nippon Gases, 5.0) was used as an adsorbate. The specific surface area (SSA) of the samples was calculated by a multipoint BET analysis (five points) in the 0.17−0.37 p/p^0 range, using the software ASiQwin.

UV−Vis Diffuse Reflectance Spectroscopy. The spectrometer employed was a UV−Vis−NIR Cary 5E equipped with an integrating sphere (Department of Chemical Sciences, University of Padova). The spectra were recorded in the range 2500−300 nm, with a scan rate of 600 nm/min and an acquisition range of 1 nm. The baseline was acquired as 100% and 0% of transmittance, while the spectra were recorded as a function of reflectance (%R). The band gap was determined based on the Kubelka−Munk function.[41]

Inductively Coupled Plasma-Mass Spectrometry. The instrument used for the ICP-MS analysis was the Agilent Technologies 7700xx (Department of Chemical Sciences, University of Padova), equipped with a 1550 W plasma power. The samples were previously subjected to mineralization with concentrated nitric acid at 65% and concentrated hydrochloric acid at 37% (1:1 w/w) by heating in a water bath for 1 h. The digested solutions thus obtained were diluted with a solution at 5% w/w of nitric acid at 65%.

X-ray Absorption Spectroscopy. XAS investigations were performed at the SAMBA beamline of the French national synchrotron facility SOLEIL (France). The acquisitions were carried out in fluorescence mode, in continuous scanning mode, using a Ge detector to detect and select the radiation emitted from the samples. A Si(220) crystal

https://doi.org/10.1021/acsanm.3c02136
ACS Appl. Nano Mater. 2023, 6, 15510−15520

monochromator was used for energy selection. The acquisition range was set to 6900−7900 eV for the Eu L_3-edge, while a range of 19800−21597 eV was employed for Mo K-edge measurements.

Photoluminescence. PL investigations were carried out using a Fluorlolog 3 (HORIBA) spectrophotometer equipped with a dual lamp housing, a 450 W short-arc Xe lamp, a UV Xe flashlamp, double-grated excitation and emission monochromators, a photomultiplier tube as a detector, and a TCSPC upgrade (Department of Inorganic and Analytical Chemistry, Justus Liebig University Giessen). Overall emission decay times were acquired with the abovementioned Fluorolog 3 using DataStation software. A Xe microsecond flashlamp was used for excitation. Exponential tail fitting was used for calculation of emission lifetime using Decay Analysis Software 6. Quality of the fit was evaluated by χ^2 value.

RESULTS AND DISCUSSION

Undoped Calcium Molybdate. All the diffraction peaks of the PXRD (Figure 1) patterns of the obtained $CaMoO_4$ are indexed according to the tetragonal body-centered scheelite-type $CaMoO_4$ structure (PDF Card No. 85-1267, space group $I4_1/a$ (88)),[23] confirming that the obtained calcium molybdate is highly crystalline and phase pure, within the detection limit of PXRD. Further confirmation of the calcium molybdate lattice structure is provided by Raman analysis in SI Section S2.4. By comparing the diffraction patterns of the samples obtained by the two different synthetic methods (Figure 1), it is worth highlighting a difference in the broadening of the reflections: in particular evidently broader diffraction peaks are found for ME CM compared to batch CM, resulting from significantly smaller coherently scattering domains (i.e., crystallites). Indeed, among other contributions, the broadening of reflections in a diffraction pattern is inversely related to the mean crystallite size. By WPPF (method described in Section S1.3 in the SI)[39,40] of PXRD patterns, the average crystallite sizes of CM are estimated to be about 8 nm and 30 nm for ME and batch samples, respectively (Figure S3 and Table S4). This relevant difference provides evidence of the effect of the CS on the crystallite size, which turns out to be considerably smaller by the ME approach than by a "macroreactor" approach without confinement. The estimated experimental lattice parameters (ME a = 5.237 Å and c = 11.455 Å; batch a = 5.233 Å and c = 11.461 Å) and the unit cell volumes agree with the ones reported in the literature for a scheelite-type structure[23,24,28,42] and are described in detail in SI Section S2.3.

Additionally, as observed in TEM micrographs (Figure 2a,b), the inverse miniemulsion approach yields the formation of fairly monodispersed spherical independent NPs with an average size of 12.0 ± 2.7 nm (polydispersity index, PDI of 0.2). On the other hand, for the sample synthesized in batch, particles are found to be of irregular shape with a wide size distribution and a larger average size of NPs of 58.0 ± 30.9 nm (PDI of 0.5) (Figure 2d,e). In the latter case, NPs tend to aggregate in oriented self-organized microstructures with an ellipsoidal-like shape[23] (SEM, Figure S5). These observations are in agreement with the hypothesized controlled and uniform crystallization processes taking place within parallel nanoreactors by ME,[43] as opposed to less controlled nucleation and growth caused by nonuniform mixing and thereby concentration gradients typical of a "macroreactor" (batch approach). Thereby, it is worth reiterating that spatial confinement is

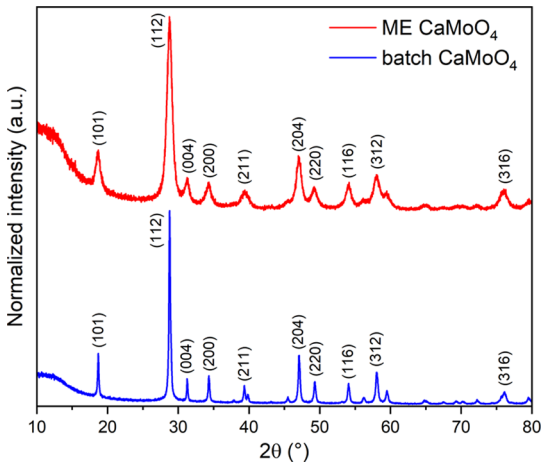

Figure 1. Normalized PXRD patterns of undoped ME (red line) and batch (blue line) samples. Miller indexes (*hkl*) of the tetragonal scheelite-type $CaMoO_4$ structure are reported. PXRD patterns are shifted vertically for clarity.

proven to play an important role in controlling size, size distribution, and morphology of CM NPs, leading to spherical independent NPs with a narrow size distribution, not observed for its batch counterpart. Finally, the SSA of undoped samples evaluated by BET (Figure S6) analysis further confirms the role of CS, already pointed out by TEM and SEM analyses (SI Section S2.5), showing substantial differences between the ME and batch samples in the size, shape, and aggregation degree of the NPs. Indeed, the ME sample shows a higher SSA with respect to the batch sample (i.e., 37 m^2/g vs 9 m^2/g, respectively), due to the fact that the sample is composed of NPs, whereas the batch sample presents larger particles aggregated in microstructures.

Further differences between the ME and batch undoped CM samples arise by considering the band gap for the direct allowed transition, extrapolated from the Tauc plot[44] (Figure 2c,f for ME and batch samples, respectively), derived from UV−Vis diffuse reflectance spectra. It is found that the band gaps for ME and batch samples are about 4.2 and 3.8 eV (i.e., 295 and 326 nm), respectively. The larger band gap obtained for the ME sample can likely be ascribed to a size effect of these ME nanostructures, as compared to the batch-derived ones, further confirming the role of space confinement on the synthesis outcome. The band gap values reported in the literature for $CaMoO_4$ can vary significantly according to the size and shape of the particles, and degree of structural distortions or defects in the lattice.[23]

To provide further evidence of the effects of the space confinement on the size and morphology of the CM nanostructures, syntheses were performed by systematically varying the concentration of the starting solutions (0.15, 0.20, 0.25, 0.50, 1.0, 1.5, and 2.0 M). In particular, by theoretical predictions,[13] a variation of the concentration of precursor solution is expected to affect the size of ME droplets, as different amounts of the osmotic agent (i.e., the precursor salt) should generate an osmotic pressure that balances out with the counteracting Laplace pressure at different nanodroplet dimensions.[7] The crystallization of phase-pure tetragonal calcium molybdate is achieved at all concentrations (PXRD patterns and WPPFs in Section S2.7 in the SI, Figures S7−S11); however, trends of average crystallite sizes as a function of the concentration of the precursors solutions are observed

https://doi.org/10.1021/acsanm.3c02136
ACS Appl. Nano Mater. 2023, 6, 15510−15520

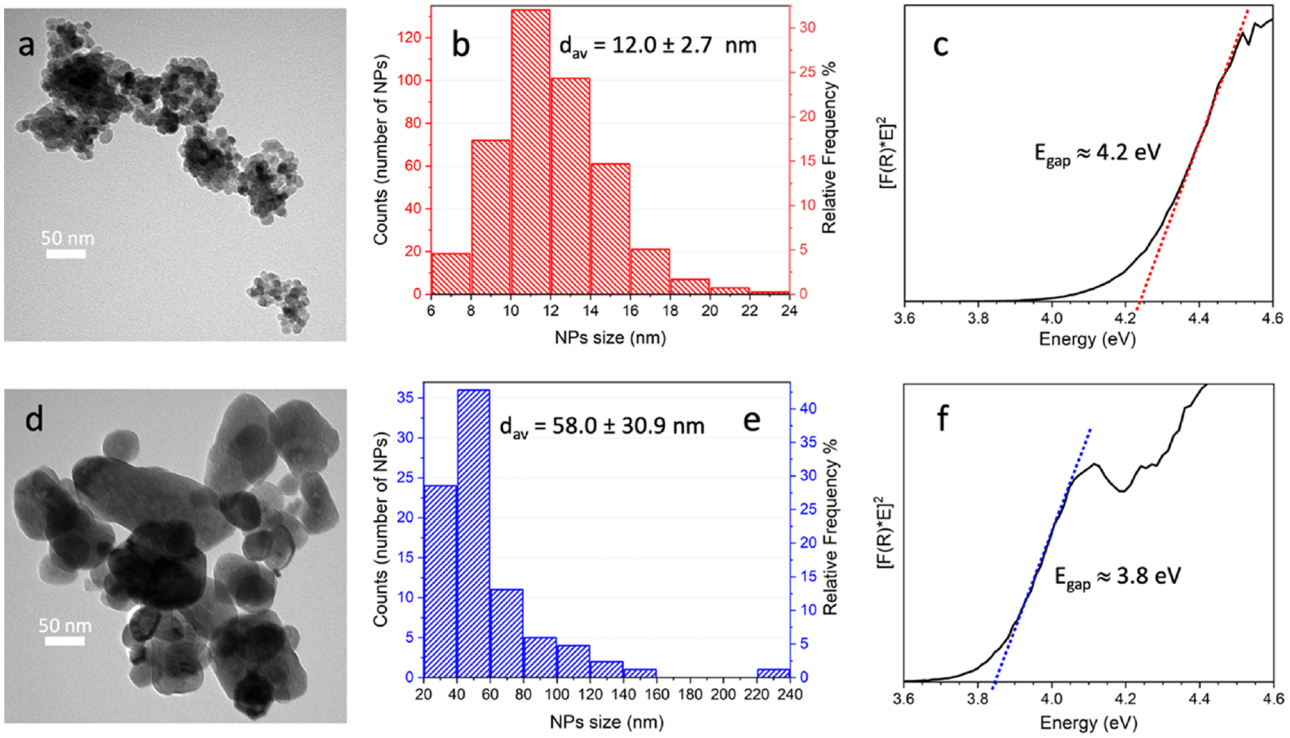

Figure 2. TEM micrographs (a,d), relative size distribution histograms (b,e), and Tauc plots from UV−Vis diffuse reflectance measurements (c,f) of undoped ME (red) and batch (blue) samples, respectively.

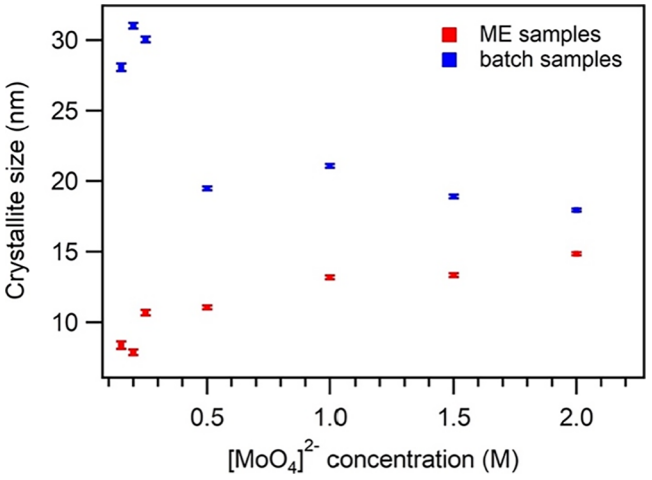

Figure 3. Average crystallite size and relative error (bars) of ME (red dots) and batch (blue dots) samples, estimated by WPPF of PXRD patterns, as a function of precursor concentration ($[MoO_4]^{2-}$:Ca^{2+} 1:1 mol).

to differ depending on the different synthetic pathways (Figure 3). In particular, the average crystallite size of calcium molybdate is found to increase accordingly with concentration for the CM samples synthesized in inverse ME CS (from about 8 nm starting with 0.15 M solutions to about 15 nm with 2.0 M solutions), whereas for the samples obtained by the batch approach, the opposite trend is observed (starting from a crystallite size of about 30 nm with 0.15 M solutions and decreasing to about 18 nm with 2.0 M solutions). The observed increasing average crystallite size for the inverse ME samples with increasing concentration of the starting precursors is also observed in a slightly increasing trend of the average NPs size and in the broadening of the size distribution, as evidenced by TEM analysis (Figures S12 and S13). These opposite behaviors can be explained by considering the different crystallization mechanisms that are involved in the two synthetic pathways. For a simple precipitation method, as reported by Packter and Chauhan[45] and Batra and Arora,[46] the number of nuclei should increase with increasing concentration of the molybdate salt and, as a consequence, the higher the nuclei concentration, the smaller will be the particles resulting from the growth process. According to LaMer burst nucleation theory,[47] with a higher starting concentration of the solute, the supersaturation condition is reached rapidly and a higher number of nuclei forms simultaneously. On the contrary, for the inverse ME synthesis, the crystallization of CM takes place in a parallel fashion inside each droplet in a constrained environment. Therefore, it can be stated that the whole precursor, which is present within a droplet, will contribute to the formation of a particle. As a consequence, when the amount of the starting material is higher, and thus also the local concentration inside the nanodroplets, larger NPs are obtained.

Eu^{3+}-Doped Calcium Molybdate. The effect of the CS is further assessed considering the doping process and Eu^{3+} insertion in the CM matrix, synthesized with different amounts of Eu^{3+} (1, 3, 5, and 7 at. % calculated as the Eu/Mo molar ratio) through the inverse miniemulsion approach, and in batch as a comparison without the space confinement. From the ICP-MS analysis (Table S8), the experimental Eu content is found to agree with the nominal one and, in addition, by comparing equal Eu content, they are similar for the samples obtained by the two synthetic methods. PXRD analysis (Figures S16 and S17) confirms the crystallization of phase-pure tetragonal CM at all the Eu amounts with both synthetic approaches. However, it is worth noticing that, for batch samples with higher Eu amounts (5 and 7 at. %), some

https://doi.org/10.1021/acsanm.3c02136
ACS Appl. Nano Mater. 2023, 6, 15510−15520

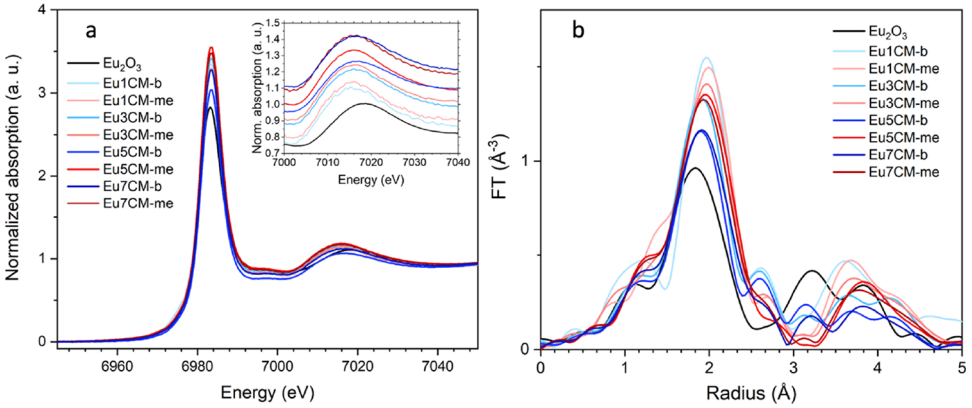

Figure 4. (a) Eu L_3-edge XANES spectra. The inset shows a zoomed-in image of the band in the range 7000−7040 eV; curves in the inset are shifted vertically for clarity. (b) Fourier transform of the k^2-weighted EXAFS functions (k = 3−10 Å^{-1}), showing the pseudoradial distribution around the Eu absorbers (not corrected for phase shift). Here, sample names end with −b and −me for batch and ME, respectively, and the digit refers to the Eu^{3+} content. As an example, sample 1 at. % Eu^{3+}:$CaMoO_4$ synthesized in ME is named Eu1CM-me.

impurities are detected from the PXRD patterns, compatible with the presence of Eu-based spurious phases, such as Eu_2O_3 and EuOOH (SI, Section S2.10).

As mentioned in the Introduction section, in the doping process, Eu^{3+} ions should replace the Ca^{2+} ions on their site (aliovalent substitution). Indeed, the ionic radius of Eu^{3+} is close to the one of Ca^{2+} in an eightfold coordination, i.e., r_{Eu3+} = 1.066 Å (in VIII coordination) and r_{Ca2+} = 1.12 Å (in VIII coordination).[48] However, as a divalent ion is substituted with a trivalent ion, to guarantee the charge neutrality in the doped systems, the most probable mechanisms occurring are the formation of Ca-site vacancies and the codoping of the matrix with Eu^{3+} and an alkaline cation A^+.[49−52] Since the synthesis of Eu^{3+}-doped CM involves a Na^+-containing molybdate precursor, it is highly reasonable that Na^+ is present in the doped samples. Nonetheless, since the scheelite structures can include a large concentration of vacancies in the Ca sublattice, the simultaneous presence of some Ca-site vacancies in these samples cannot be excluded.[53]

From the fitting of the powder diffractograms of ME doped samples, a slight increase in the cell volume with increasing Eu content can be observed (Figure S20), more appreciable for the sample with a higher amount of Eu (7 at. %). This slight expansion of the unit cell volume[49,54] can be explained considering two factors: (i) the higher charge and smaller ionic radius of Eu^{3+}, as compared to Ca^{2+}, which entails a decrease in the Eu−O distance and an increase in the MoO_4 tetrahedron volume and (ii) the presence of Na^+ into the structure, having a Na^+ ionic radius larger than Ca^{2+} (r_{Na+} = 1.18 Å in VIII coordination).[48] On the contrary, in the case of the batch samples, no significant variation of the unit cell volume as a function of the Eu level is evident. Thus, confining the synthesis of doped CM within ME nanodroplets seems to favor a controlled substitution of Eu in the Ca site, as no Eu-based impurities in ME samples are evident in the diffractograms and a slight expansion of scheelite unit cell upon the statistic replacement with Eu is observed.

By considering the TEM micrographs (Figure S22), the ME nanodroplets are proven again to be efficient in maintaining the quite-spherical morphology of NPs even during the doping process. On the contrary, for the doped batch samples (Figure S23), both sheet-like and quite regular spindle-like microstructures of around 2 μm are clearly distinguishable (SI Section S2.11).

To further elucidate the details of the structure and chemical environment around Mo and Eu ions, X-ray absorption experiments were performed at both Eu L_3- and Mo K-edges. The reported spectra (Figure 4a) are normalized to eliminate possible concentration effects, as well as variations due to differences in sample preparation and/or thickness and instrumental effects. Compared to the Eu_2O_3 reference, the Eu L_3-edge X-ray absorption near edge structure (XANES) spectra of the samples all show a higher intensity of the white line (maximum intensity at 6984 eV, see Figure 4a). Since the intensity of this maximum is influenced by the splitting of the empty d orbitals (the white line arises from the transition of the $2p_{3/2}$ electrons to unfilled d orbitals), differences in this regard indicate a variation in the crystalline environment around the Eu absorbers.[55] Furthermore, a second band is found at 7016 eV (see inset in Figure 4a), while for the oxide reference, this is shifted at 7019 eV, as additional evidence of the different structures. The only exception is the batch sample with 5 at. % Eu content, for which the white line shows a decrease in intensity and the second band lays at an intermediate position (7017.4 eV). Most likely this is the result of the presence of Eu_2O_3 moieties in the sample. When comparing ME and batch samples, the former shows more intense bands, indicating a less disordered environment.

The Fourier transforms of the corresponding extended X-ray absorption fine structure (EXAFS) curves at the Eu L_3-edge once more evidence the difference between the reference oxide and the doped samples since, for the latter ones, the position of the first backscattering contributions (Eu−O, at around 2 Å in Figure 4b) is shifted toward longer R-values and its intensity is increased. From Figure 4b, it can be seen that overall, the ME samples show a more intense shell with respect to the batch counterpart, which may be traced back to a considerably lower disorder in the structure. In general, both for ME and batch samples, the intensity decreases with increasing Eu concentration. This latter effect, coupled with an increase in the Debye−Waller factor (DW) as a function of the Eu content, might be a consequence of an increased disorder in the Eu sites, due to the presence of a higher amount of Eu in the samples. For the batch samples, the larger variation of the DW factor with increasing Eu amounts might be ascribed to the presence of different Eu-based spurious species, in addition to the substituted Eu in the Ca sites.

https://doi.org/10.1021/acsanm.3c02136
ACS Appl. Nano Mater. 2023, 6, 15510−15520

Table 1. Results of the First-Shell Fitting, in the *R*-Space, of the k^2-Weighted EXAFS Curves (Eu L_3-edge, k = 3−10 $Å^{-1}$)

europium content	sample	Eu−O (Å)	coordination number	DW (10^{-3} $Å^2$)	E_0 (eV)	*R*-factor (%)
1 at. %	Eu1CM-me	2.42 ± 0.01	8.4 ± 1.6	7.0 ± 3.4	5.89 ± 1.81	1.9
	Eu1CM-b	2.43 ± 0.02	7.0 ± 1.8	4.1 ± 2.7	7.13 ± 2.34	3.3
3 at. %	Eu3CM-me	2.42 ± 0.01	8.1 ± 1.1	7.5 ± 2.4	5.77 ± 1.28	0.6
	Eu3CM-b	2.39 ± 0.02	7.8 ± 1.2	8.0 ± 2.8	3.72 ± 1.59	1.8
5 at. %	Eu5CM-me	2.42 ± 0.01	8.5 ± 1.6	8.7 ± 3.5	5.16 ± 1.85	2.7
	Eu5CM-b	2.38 ± 0.02	6.5 ± 1.0	8.4 ± 2.6	3.15 ± 1.52	2.0
7 at. %	Eu7CM-me	2.41 ± 0.01	8.3 ± 1.2	9.1 ± 2.5	4.93 ± 1.39	0.5
	Eu7CM-b	2.40 ± 0.01	8.3 ± 1.0	11.0 ± 2.3	3.94 ± 1.19	1.1

Fitting of the EXAFS functions (Table 1) evidences that, for the ME samples, the Eu coordination is about 8, compatible with a substitution in Ca^{2+} sites.[54,56] In addition, the Eu−O distance is close to that reported for Ca−O (2.46 Å),[54] with a small difference due to the higher charge and smaller ionic radius of Eu^{3+}. At the same time, this distance is significantly larger than that typically found for Eu_2O_3 (ca. 2.33 Å). Overall, the results for ME samples seem to confirm that Eu efficiently substitutes Ca at all the investigated concentrations. The picture for batch samples is more complex. At the lowest concentration, the Eu−O distance seems to be compatible with a substitutional replacement, but as the Eu content increases, this bond distance decreases. Even though the difference between the two sets of samples is not big, it is still significant. In the case of the batch sample with 5 at. % Eu, already showing a different XANES, a lower coordination number is observed. This might be traced back to the presence of small clusters of Eu_2O_3, also evidenced by PXRD fitting, and/or a second Eu-containing species. On the other hand, the 7 at. % batch sample presents a higher coordination number with respect to the 5 at. % batch sample, and it is thus possible that it contains only a second species, possibly EuOOH, also having a coordination number of 8 around the Eu absorber and already detected by WPPF of PXRD patterns (SI Section S2.10).

The Mo K-edge XANES spectra (SI Section S2.13) give evidence that molybdenum is in tetrahedral coordination (cf. Figure S25) and the Eu^{3+}-doped samples closely resemble the spectrum of the undoped crystalline CM, highlighting that the presence of the europium ions does not significantly alter the local structure around molybdenum, at least within the experimental error. However, a longer Mo−O distance for all the doped samples (1.79 ± 0.01 Å) compared to that of the undoped CM (1.77 ± 0.01 Å) can be noticed (cf. Table S11), thus confirming the postulated unit cell volume expansion as a consequence of the doping process.

Optical Properties of Eu^{3+}-Doped Calcium Molybdate. In order to assess the effect of miniemulsion droplet spatial confinement on the functional properties of the synthesized material, as well as further study the doping mechanism, the optical absorption and PL properties of Eu^{3+}-doped CM samples are investigated. The optical absorption properties of the samples were explored using UV−Vis DRS. The estimated band gap value for the Eu-doped samples at all the Eu contents and synthesized by both synthetic approaches is in the range of 3.8−3.9 eV (Figure S24). A slight decrease of the band gap value as a function of an increasing doping percentage is found for ME samples (from 3.9 eV for the 1 at. % doped sample to 3.8 eV for the 7 at. % doped one), likely ascribed to a higher degree of distortions in the lattice with increased Eu content. On the other hand, as no trend in the band gap values for batch samples is evidenced, the band gap values are independent on the Eu amount. Considering also the fact that, for the batch samples, the doping with Eu^{3+} ions does not modify significantly the band gap value as compared to the undoped one (3.8 eV), a not effective substitutional replacement of Eu^{3+} in the host matrix could be hinted.

The investigation of the PL properties discloses further details on the doping mechanism. The emission spectra of Eu^{3+}-doped CM, monitored by exciting the CM matrix at 217 nm, show the characteristic transitions of Eu^{3+}, which are dominant. The excitation and emission spectra of the 3 at. % ME sample measured at RT are reported as an example in Figure 5a (spectra for all samples are in SI Section S2.15 and Figures S27−S42). Going more into detail, the Eu^{3+}:$CaMoO_4$ system undergoes two excitation processes: a broad matrix-based band in the UV region indicating an energy transfer from the CM matrix to Eu^{3+} and additional narrow-lined direct *f*−*f* transitions of Eu^{3+}. The relative intensity of both excitation processes differs significantly by comparing the excitation spectra of doped samples synthesized by the two different approaches (Figure 5b). For ME-doped samples, a trend can be observed: with an increase of the Eu^{3+} amount in the sample, the relative intensity of direct *f*−*f* excitation increases (Table S21). This is a result of the shorter distance between Eu^{3+} centers at higher concentrations, leading to a higher energy transfer between lanthanide ions. On the contrary, for batch samples, no such trend can be observed: the relative intensity of direct *f*−*f* excitation is quite constant despite the different contents of Eu in the sample, assessed by ICP-MS, indicating that likely the average distance between Eu^{3+} ions is constant too. Moreover, being the relative intensity higher than that for ME samples at all the Eu content investigated, it can be supposed that, for the ME samples, the Eu^{3+} distribution is more homogeneous, while for the batch samples sites with local Eu^{3+} concentration higher than the nominal Eu content are likely present.

The emission of all Eu^{3+}-containing samples investigated at RT consists of typical $^5D_0 \rightarrow {}^7F_J$ (J = 0−4) transitions, with the hypersensitive $^5D_0 \rightarrow {}^7F_2$ being the most intense one. As almost no emission intensity is observed from the molybdate matrix, a quite efficient energy transfer to europium can be stated. For most of the samples investigated, the emission profiles do not depend on the excitation pathway. Exceptions for this are batch samples with 5 and 7 at. % Eu amounts, for which, upon an excitation wavelength of 393 nm (Eu^{3+} based excitation, $^5L_6 \leftarrow {}^7F_0$), additional narrow lines appear in the emission, especially noticeable for $^5D_0 \rightarrow {}^7F_2$ and $^5D_0 \rightarrow {}^7F_4$ transitions (Figures S38 and S42). This indicates that these two samples have Eu^{3+}-based spectroscopically active impurities, in agreement with the presence of Eu_2O_3 or EuOOH hypothesized from XAS analysis and PXRD fitting. Indeed,

https://doi.org/10.1021/acsanm.3c02136
ACS Appl. Nano Mater. 2023, 6, 15510−15520

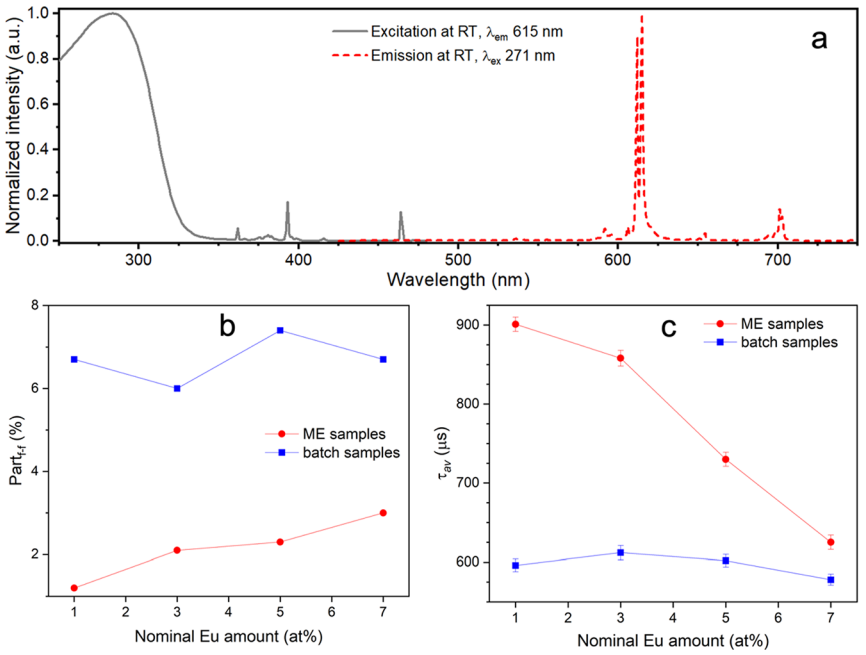

Figure 5. (a) Solid state normalized excitation and emission spectra of Eu3CM-me (ME 3 at. % Eu^{3+}:$CaMoO_4$) measured at RT. Matrix-based measurement (dashed line, emission spectrum λ_{ex} 271 nm) and Eu^{3+} transition-based measurement (solid line, excitation spectrum λ_{em} 615). (b) Ratio of integrated direct Eu^{3+} excitation to the sum of integrated excitation at RT: λ_{em} = 615 nm, excitation through the $CaMoO_4$ matrix integrated from 250 to 355 nm and direct Eu^{3+} f−f excitation integrated from 355 to 545 nm and (c) average Eu^{3+} emission lifetime at RT upon excitation through the host matrix (λ_{ex} = 271 nm and λ_{em} = 615 or 703 nm) of ME (red) and batch (blue) samples.

both Eu_2O_3 and EuOOH are spectroscopically active. No spectroscopical impurities are observed for the other samples.

Since for all samples investigated the observed *f*−*f* transitions $^5D_0 \rightarrow {}^7F_J$ (J = 0−4) are well resolved, it can be concluded that Eu^{3+} occupies a defined crystallographic position in the CM matrix, i.e., the positions of Ca^{2+}. Weak $^5D_0 \rightarrow {}^7F_0$ transition, splitting of transitions (two lines for $^5D_0 \rightarrow {}^7F_1$ transition and four for $^5D_0 \rightarrow {}^7F_2$), and a high ratio of a forced electric dipole to a magnetic dipole ($R^{0-2}/_{0-1}$, 14.5−16.4 for all samples) indicate that Eu^{3+} has a tetragonal local symmetry, though not C_4 or C_{4v}.[57,58] As confirmation, a coordination number of Eu of 8 for the ME samples as calculated from the EXAFS analysis fits with the tetragonal symmetry. In addition, if the EuO_8 cluster takes on a cuboctahedral conformation similar to CaO_8 (which, being distorted, should not have C_4 or C_{4v} symmetry), then this is also compatible with the more intense and narrower white line from XAS analysis for the ME samples.

A detailed discussion of the determined quantum yield values and absolute emission intensities for the ME and batch Eu^{3+}-doped samples is given in SI Section S2.17. In general, it is possible to highlight that ME samples, compared to the batch ones, have a higher emission intensity by 9−16%, although showing lower QY (Figure S52 and Table S21). To understand this contradicting observation, the sample light absorption needs also to be considered. ME samples absorb about 5−10% more light as compared to the batch ones (UV−Vis DRS, Figure S24c,d). This means that ME doped samples emit more light relative to the amount of light irradiated on the substance.

To acquire further knowledge of the PL mechanism, overall emission process decay times were determined at RT and at 77 K for $CaMoO_4$ and Eu^{3+}-based processes (Figure 5c). For all samples investigated, the overall emission decay process can be fitted only with a minimum of two exponential functions. This indicates the large influence of the surface, and it is quite normal for NPs due to the high surface-to-volume ratio.[59,60] Full data on emission decay fit parameters for all investigations carried out at RT and 77 K are given in SI Section S2.16 (Tables S12 and S20). Measured average lifetimes are somewhat shorter than that for typical Eu^{3+}-doped systems (3.8−8.8 ms),[61−63] but are in the range of other Eu^{3+} containing scheelites (0.3−0.9 ms).[53,64] The Eu^{3+} overall emission decay process time in ME samples depends on the Eu^{3+} content and varies from 0.901 ± 0.009 ms for the 1 at. % doped sample down to 0.625 ± 0.009 ms for the 7 at. % sample (Table S21). The decrease of the emission lifetime is a direct result of the higher Eu^{3+} content homogeneously distributed into the host matrix, as the distance between two emissive centers shortens, and therefore the nonradiative de-excitation has a higher probability through a cross-relaxation process.[61,65,66] On the other hand, for the batch samples, the emission lifetime, which is 0.60 ± 0.02 ms for all samples (Table S21), does hardly depend on the Eu^{3+} content. This implies a nonuniform distribution of europium ions in the host matrix, as the concentration quenching for all samples is quite the same. This confirms again the heterogeneity of batch samples regarding the presence of a locally higher Eu^{3+} concentration than the average, macroscopic experimental Eu^{3+} amount, assessed by ICP-MS. Thus, the decreasing trend in the emission lifetime with increasing Eu content for the ME samples and the absence of such a trend for the batch samples, allow confirming the effect of ME nanodroplet spatial confinement on the Eu^{3+} distribution in the matrix, leading to a more homogeneous one. These results demonstrate that, by confining the crystallization of calcium molybdate within ME nanodroplets, tight control on the synthesis outcome can

https://doi.org/10.1021/acsanm.3c02136
ACS Appl. Nano Mater. 2023, 6, 15510−15520

be achieved, with relevant consequences on the functional properties.

CONCLUSIONS

The exploitation of a constrained environment to efficiently control the final outcome of a synthesis is demonstrated to be a very promising approach to obtain inorganic materials with defined size, morphology, and functional properties. Herein, we successfully investigate the effect of the inverse ME nanodroplets' space confinement on the synthesis of calcium molybdate nanostructures. A systematic comparison of the features of the samples obtained from the inverse ME with those obtained via batch synthesis (without a constraint environment) indicates how the CS is an effective tool in the synthesis of this target inorganic material. As a result, when synthesized within the ME nanodroplets, calcium molybdate displays a smaller average crystallite size (8 nm vs 30 nm) and smaller, not aggregated and more monodispersed NPs (around 12 nm with a PDI of 0.2 vs 58 nm with a PDI of 0.5) with a regular spherical morphology, as opposed to irregularly shaped batch NPs aggregating into mesostructures. All these aspects are ascribable to the supposed uniform and controlled crystallization occurring inside each nanodroplet, as opposed to the less controlled nucleation and growth for a classic nonconfined approach. As further evidence of the different crystallization pathway, which takes place in the CS, we can highlight how a different nucleation and growth mechanism is likely involved by considering the opposite trend observed in the average crystallite size upon variation of the precursor starting concentration in the synthesis of calcium molybdate with and without the confinement.

Furthermore, the space confinement plays a pivotal role in the doping process of the calcium molybdate matrix with Eu^{3+} ions, leading to a more homogeneous distribution of Eu^{3+} into the host matrix, without the presence of segregation even at higher Eu^{3+} amounts, as confirmed by PL, PXRD, and XAS analyses, and as opposed to what is observed for the batch counter investigation.

Accordingly, the inverse miniemulsion approach can be a real step forward toward a more homogenous and controlled statistic replacement when considering the fabrication of doped inorganic materials. Thus, inverse ME is an effective route for a confined environment for the synthesis of inorganic NPs, especially allowing a uniform crystallization and precise control of the size and shape of NPs as well as ensuring a homogeneous doping process for the development of photoluminescent materials with tunable final features.

ASSOCIATED CONTENT

Supporting Information

The Supporting Information is available free of charge at https://pubs.acs.org/doi/10.1021/acsanm.3c02136.

Experimental and characterization technique details, WPPF of PXRD patterns, Raman analyses, TEM and SEM images, N_2-physisorption isotherms, ICP-MS data, XAS data at the Mo K-edge, and additional and detailed PL results (PDF)

AUTHOR INFORMATION

Corresponding Authors

Klaus Müller-Buschbaum − *Institute for Inorganic and Analytical Chemistry, Justus-Liebig-University Giessen, 35392 Giessen, Germany; Center for Materials Research (LAMA), Justus-Liebig-University Giessen, 35392 Giessen, Germany;* orcid.org/0000-0002-2857-8379; Email: kmbac@uni-giessen.de

Silvia Gross − *Department of Chemical Sciences, University of Padova, 35131 Padova, Italy; Institute for Chemical Technology and Polymer Chemistry (ITCP), Karlsruhe Institute of Technology (KIT), 76131 Karlsruhe, Germany;* orcid.org/0000-0003-1860-8711; Email: silvia.gross@unipd.it

Authors

Chiara Mazzariol − *Department of Chemical Sciences, University of Padova, 35131 Padova, Italy; Institute for Inorganic and Analytical Chemistry, Justus-Liebig-University Giessen, 35392 Giessen, Germany;* orcid.org/0000-0003-4394-3589

Francesca Tajoli − *Department of Chemical Sciences, University of Padova, 35131 Padova, Italy;* orcid.org/0000-0002-6416-6638

Alexander E. Sedykh − *Institute for Inorganic and Analytical Chemistry, Justus-Liebig-University Giessen, 35392 Giessen, Germany;* orcid.org/0000-0003-2650-5173

Paolo Dolcet − *Institute for Chemical Technology and Polymer Chemistry (ITCP), Karlsruhe Institute of Technology (KIT), 76131 Karlsruhe, Germany;* orcid.org/0000-0001-9583-9375

Jan-Dierk Grunwaldt − *Institute for Chemical Technology and Polymer Chemistry (ITCP), Karlsruhe Institute of Technology (KIT), 76131 Karlsruhe, Germany; Institute of Catalysis Research and Technology (IKFT), Karlsruhe Institute of Technology (KIT), 76344 Eggenstein-Leopoldshafen, Germany;* orcid.org/0000-0003-3606-0956

Complete contact information is available at: https://pubs.acs.org/10.1021/acsanm.3c02136

Notes

The authors declare no competing financial interest.

ACKNOWLEDGMENTS

We gratefully thank Dr. Federico Caicci and Dr. Francesco Boldrin (Department of Biology, University of Padova) and Prof. Denis Badocco and Prof. Paolo Pastore (Department of Chemistry, University of Padova) for TEM and ICP-MS analyses, respectively. Dr. Emiliano Fonda (SAMBA beamline, SOLEIL synchrotron) is kindly acknowledged for technical assistance. Soleil synchrotron (proposal 20201498) is acknowledged for providing synchrotron beamtime. F.T. kindly acknowledges the PhD Course in Molecular Sciences of University of Padova for funding. S.G. acknowledges the DAAD for financial support for a research stay at the Justus-Liebig-Universität Giessen in Summer 2021 and additionally thanks for a Mercator Fellow position at KIT funded by the Deutsche Forschungsgemeinschaft (DFG, German Research Foundation) within SFB 1441—Project-ID 426888090. S.G. acknowledges the Interdepartmental Centre Giorgio Levi Cases for Energy Economics and Technology of the University of Padova for the funding of the project AMON-RA and the project P-DiSC (P-DiSC #05BIRD2018-UNIPD) "Space Matters: crystallization of inorganic nanostructures in confined spaces" of the University of Padova. K.M.-B. acknowledges the Deutsche Forschungsgemeinschaft for support within the

project "Formation and properties of opto-magnetic hybrid materials via the influence of external stimuli" (MU-1562/7-2).

REFERENCES

(1) Polarz, S. Shape Matters: Anisotropy of the Morphology of Inorganic Colloidal Particles - Synthesis and Function. *Adv. Funct. Mater.* **2011**, *21*, 3214−3230.

(2) Jiang, Q.; Ward, M. D. Crystallization under Nanoscale Confinement. *Chem. Soc. Rev.* **2014**, *43*, 2066−2079.

(3) Petrosko, S. H.; Johnson, R.; White, H.; Mirkin, C. A. Nanoreactors: Small Spaces, Big Implications in Chemistry. *J. Am. Chem. Soc.* **2016**, *138*, 7443−7445.

(4) Moilanen, D. E.; Levinger, N. E.; Spry, D. B.; Fayer, M. D. Confinement or the Nature of the Interface? Dynamics of Nanoscopic Water. *J. Am. Chem. Soc.* **2007**, *129*, 14311−14318.

(5) Fröba, M.; Köhn, R.; Bouffaud, G.; Richard, O.; van Tendeloo, G. Fe_2O_3 Nanoparticles within Mesoporous MCM-48 Silica: In Situ Formation and Characterization. *Chem. Mater.* **1999**, *11*, 2858−2865.

(6) Desbiens, N.; Demachy, I.; Fuchs, A. H.; Kirsch-Rodeschini, H.; Soulard, M.; Patarin, J. Water Condensation in Hydrophobic Nanopores. *Angew. Chem., Int. Ed.* **2005**, *44*, 5310−5313.

(7) Landfester, K. Synthesis of Colloidal Particles in Miniemulsions. *Annu. Rev. Mater. Res.* **2006**, *36*, 231−279.

(8) Montenegro, R.; Antonietti, M.; Mastai, Y.; Landfester, K. Crystallization in Miniemulsion Droplets. *J. Phys. Chem. B* **2003**, *107*, 5088−5094.

(9) Wang, K.; Jordan, J. H.; Hu, X.; Wang, L. Supramolecular Strategies for Controlling Reactivity within Confined Nanospaces. *Angew. Chem., Int. Ed.* **2020**, *59*, 13712−13721.

(10) Ha, J.-M.; Wolf, J. H.; Hillmyer, M. A.; Ward, M. D. Polymorph Selectivity under Nanoscopic Confinement. *J. Am. Chem. Soc.* **2004**, *126*, 3382−3383.

(11) Hamilton, B. D.; Ha, J.-M.; Hillmyer, M. A.; Ward, M. D. Manipulating Crystal Growth and Polymorphism by Confinement in Nanoscale Crystallization Chambers. *Acc. Chem. Res.* **2012**, *45*, 414−423.

(12) Mietner, J. B.; Brieler, F. J.; Lee, Y. J.; Fröba, M. Properties of Water Confined in Periodic Mesoporous Organosilicas: Nanoimprinting the Local Structure. *Angew. Chem., Int. Ed.* **2017**, *56*, 12348−12351.

(13) Landfester, K. Miniemulsions for Nanoparticle Synthesis. In *Colloid Chemistry II. Topics in Current Chemistry*; Antonietti, M., Ed.; Springer Berlin: Heidelberg, 2003; Vol *227*; pp. 75−123.

(14) Landfester, K.; Antonietti, M. Miniemulsions for the Convenient Synthesis of Organic and Inorganic Nanoparticles and"Single Molecule" Applications in Materials Chemistry. In *Colloids and Colloid Assemblies*; Wiley Online Books; Wiley-VCH Verlag GmbH & Co. KGaA: Weinheim, FRG, 2003; pp 175−215.

(15) Landfester, K. Recent Developments in Miniemulsions — Formation and Stability Mechanisms. *Macromol. Symp.* **2000**, *150*, 171−178.

(16) Muñoz-Espí, R.; Landfester, K. Low-Temperature Miniemulsion-Based Routes for Synthesis of Metal Oxides. *Chem. – Eur. J.* **2020**, *26*, 9304−9313.

(17) Dolcet, P.; Maurizio, C.; Casarin, M.; Pandolfo, L.; Gialanella, S.; Badocco, D.; Pastore, P.; Speghini, A.; Gross, S. An Effective Two-Emulsion Approach to the Synthesis of Doped ZnS Crystalline Nanostructures. *Eur. J. Inorg. Chem.* **2015**, *2015*, 706−714.

(18) Dolcet, P.; Latini, F.; Casarin, M.; Speghini, A.; Tondello, E.; Foss, C.; Diodati, S.; Verin, L.; Motta, A.; Gross, S. Inorganic Chemistry in a Nanoreactor: Doped ZnO Nanostructures by Miniemulsion. *Eur. J. Inorg. Chem.* **2013**, *2013*, 2291−2300.

(19) Dolcet, P.; Casarin, M.; Maccato, C.; Bovo, L.; Ischia, G.; Gialanella, S.; Mancin, F.; Tondello, E.; Gross, S. Miniemulsions as Chemical Nanoreactors for the Room Temperature Synthesis of Inorganic Crystalline Nanostructures: ZnO Colloids. *J. Mater. Chem.* **2012**, *22*, 1620−1626.

(20) Dolcet, P.; Mambrini, A.; Pedroni, M.; Speghini, A.; Gialanella, S.; Casarin, M.; Gross, S. Room Temperature Crystallization of Highly Luminescent Lanthanide-Doped CaF_2 in Nanosized Droplets: First Example of the Synthesis of Metal Halogenide in Miniemulsion with Effective Doping and Size Control. *RSC Adv.* **2015**, *5*, 16302−16310.

(21) Antonello, A.; Jakob, G.; Dolcet, P.; Momper, R.; Kokkinopoulou, M.; Landfester, K.; Muñoz-Espí, R.; Gross, S. Synergy of Miniemulsion and Solvothermal Conditions for the Low-Temperature Crystallization of Magnetic Nanostructured Transition-Metal Ferrites. *Chem. Mater.* **2017**, *29*, 985−997.

(22) Tajoli, F.; Massagrande, M. V.; Muñoz-Espí, R.; Gross, S. Exploring the Role of Miniemulsion Nanodroplet Confinement on the Crystallization of MoO_3: Morphology Control and Insight on Crystal Formation by In Situ Time-Resolved SAXS/WAXS. *Nanomaterials* **2023**, *13*, 1046.

(23) Marques, V. S.; Cavalcante, L. S.; Sczancoski, J. C.; Alcântara, A. F. P.; Orlandi, M. O.; Moraes, E.; Longo, E.; Varela, J. A.; Siu Li, M.; Santos, M. R. M. C. Effect of Different Solvent Ratios (Water/Ethylene Glycol) on the Growth Process of $CaMoO_4$ Crystals and Their Optical Properties. *Cryst. Growth Des.* **2010**, *10*, 4752−4768.

(24) Longo, V. M.; De Figueiredo, A. T.; Campos, A. B.; Espinosa, J. W. M.; Hernandes, A. C.; Taft, C. A.; Sambrano, J. R.; Varela, J. A.; Longo, E. Different Origins of Green-Light Photoluminescence Emission in Structurally Ordered and Disordered Powders of Calcium Molybdate. *J. Phys. Chem. A* **2008**, *112*, 8920−8928.

(25) Groenink, J. A.; Hakfoort, C.; Blasse, G. The Luminescence of Calcium Molybdate. *Phys. Status Solidi A* **1979**, *54*, 329−336.

(26) Thongtem, T.; Kungwankunakorn, S.; Kuntalue, B.; Phuruangrat, A.; Thongtem, S. Luminescence and Absorbance of Highly Crystalline $CaMoO_4$, $SrMoO_4$, $CaWO_4$ and $SrWO_4$ Nanoparticles Synthesized by Co-Precipitation Method at Room Temperature. *J. Alloys Compd.* **2010**, *506*, 475−481.

(27) Parchur, A. K.; Ningthoujam, R. S.; Rai, S. B.; Okram, G. S.; Singh, R. A.; Tyagi, M.; Gadkari, S. C.; Tewari, R.; Vatsa, R. K. Luminescence Properties of Eu^{3+} Doped $CaMoO_4$ Nanoparticles. *Dalton Trans.* **2011**, *40*, 7595−7601.

(28) Laguna, M.; Nuñez, N. O.; Becerro, A. I.; Ocaña, M. Morphology Control of Uniform $CaMoO_4$ Microarchitectures and Development of White Light Emitting Phosphors by Ln Doping (Ln = Dy^{3+}, Eu^{3+}). *CrystEngComm* **2017**, *19*, 1590−1600.

(29) Verma, A.; Sharma, S. K. Rare-Earth Doped/Codoped $CaMoO_4$ Phosphors: A Candidate for Solar Spectrum Conversion. *Solid State Sci.* **2019**, *96*, No. 105945.

(30) Bharat, L. K.; Raju, G. S. R.; Yu, J. S. Red and Green Colors Emitting Spherical-Shaped Calcium Molybdate Nanophosphors for Enhanced Latent Fingerprint Detection. *Sci. Rep.* **2017**, *7*, 11571.

(31) Lei, F.; Yan, B. Hydrothermal Synthesis and Luminescence of $CaMO_4$:RE^{3+} (M = W, Mo; RE = Eu, Tb) Submicro-Phosphors. *J. Solid State Chem.* **2008**, *181*, 855−862.

(32) Li, J.; Zhu, G.; Zhang, T.; Zheng, H. Investigation on the Synthesis and Photoluminescence of $CaMoO_4$:Eu^{3+} Microspheres. *J. Nanosci. Nanotechnol.* **2016**, *16*, 3935−3939.

(33) Ryu, J. H.; Yoon, J. W.; Lim, C. S.; Oh, W. C.; Shim, K. B. Microwave-Assisted Synthesis of $CaMoO_4$ Nano-Powders by a Citrate Complex Method and Its Photoluminescence Property. *J. Alloys Compd.* **2005**, *390*, 245−249.

(34) Ho Ryu, J.; Geun Choi, B.; Yoon, J. W.; Bo Shim, K.; Machi, K.; Hamada, K. Synthesis of $CaMoO_4$ Nanoparticles by Pulsed Laser Ablation in Deionized Water and Optical Properties. *J. Lumin.* **2007**, *124*, 67−70.

(35) Song, J.; Xu, L.; Li, H.; Wang, Y.; He, D.; Jiao, H. Morphology-Controlled Synthesis of Eu^{3+}-Doped Calcium Molybdate Red Phosphors via a Facile Room Temperature Precipitation Route. *Powder Technol.* **2014**, *254*, 527−537.

(36) Yang, Y.; Li, X.; Feng, W.; Yang, W.; Li, W.; Tao, C. Effect of Surfactants on Morphology and Luminescent Properties of $CaMoO_4$:Eu^{3+} Red Phosphors. *J. Alloys Compd.* **2011**, *509*, 845−848.

(37) Yin, Y.; Gao, Y.; Sun, Y.; Zhou, B.; Ma, L.; Wu, X.; Zhang, X. Synthesis and Photoluminescent Properties of $CaMoO_4$ Nanostructures at Room Temperature. *Mater. Lett.* **2010**, *64*, 602−604.

https://doi.org/10.1021/acsanm.3c02136
ACS Appl. Nano Mater. 2023, 6, 15510−15520

(38) Gong, Q.; Qian, X.; Zhu, Z. Large-Scale Fabrication of Novel Hierarchical 3D $CaMoO_4$ and $SrMoO_4$ Mesocrystals via a Microemulsion-Mediated Route. *Cryst. Growth Des.* **2006**, *6*, 1821−1825.
(39) Scardi, P.; Leoni, M. Whole Powder Pattern Modelling. *Acta Crystallogr., Sect. A: Found. Crystallogr.* **2002**, *58*, 190−200.
(40) Leoni, M.; Di Maggio, R.; Polizzi, S.; Scardi, P. X-Ray Diffraction Methodology for the Microstructural Analysis of Nanocrystalline Powders: Application to Cerium Oxide. *J. Am. Ceram. Soc.* **2004**, *87*, 1133−1140.
(41) Kubelka, P.; Munk, F. A Contribution to the Optics of Pigments. *Z. Technol. Phys.* **1931**, *12*, 593−599.
(42) Minakshi, M.; Mitchell, D. R. G.; Baur, C.; Chable, J.; Barlow, A. J.; Fichtner, M.; Banerjee, A.; Chakraborty, S.; Ahuja, R. Phase Evolution in Calcium Molybdate Nanoparticles as a Function of Synthesis Temperature and Its Electrochemical Effect on Energy Storage. *Nanoscale Adv.* **2019**, *1*, 565−580.
(43) Muñoz-Espí, R.; Weiss, C. K.; Landfester, K. Inorganic Nanoparticles Prepared in Miniemulsion. *Curr. Opin. Colloid Interface Sci.* **2012**, *17*, 212−224.
(44) Makuła, P.; Pacia, M.; Macyk, W. How To Correctly Determine the Band Gap Energy of Modified Semiconductor Photocatalysts Based on UV-Vis Spectra. *J. Phys. Chem. Lett.* **2018**, *9*, 6814−6817.
(45) Packter, A.; Chauhan, P. The Precipitation of Alkaline-earth Metal and Transition Metal 'Oxinate' Powders from Aqueous Solution. Crystal Numbers and Final Sizes. *Krist. Tech.* **1975**, *10*, 995−1002.
(46) Batra, N. M.; Arora, S. K. Kinetics of Calcium Molybdate Crystallization. *Bull. Mater. Sci.* **1986**, *8*, 489−496.
(47) LaMer, V. K.; Dinegar, R. H. Theory, Production and Mechanism of Formation of Monodispersed Hydrosols. *J. Am. Chem. Soc.* **1950**, *72*, 4847−4854.
(48) Shannon, R. D. Revised Effective Ionic Radii and Systematic Studies of Interatomic Distances in Halides and Chalcogenides. *Acta Crystallogr., Sect. A: Cryst. Phys., Diffr., Theor. Gen. Crystallogr.* **1976**, *32*, 751−767.
(49) Su, Y.; Li, L.; Li, G. Synthesis and Optimum Luminescence of $CaWO_4$-Based Red Phosphors with Codoping of Eu^{3+} and Na^+. *Chem. Mater.* **2008**, *20*, 6060−6067.
(50) Liu, J.; Lian, H.; Shi, C. Improved Optical Photoluminescence by Charge Compensation in the Phosphor System $CaMoO_4$:Eu^{3+}. *Opt. Mater.* **2007**, *29*, 1591−1594.
(51) Abakumov, A. M.; Morozov, V. A.; Tsirlin, A. A.; Verbeeck, J.; Hadermann, J. Cation Ordering and Flexibility of the BO_4^{2-} Tetrahedra in Incommensurately Modulated $CaEu_2(BO_4)_4$ (B = Mo, W) Scheelites. *Inorg. Chem.* **2014**, *53*, 9407−9415.
(52) Morozov, V. A.; Lazoryak, B. I.; Shmurak, S. Z.; Kiselev, A. P.; Lebedev, O. I.; Gauquelin, N.; Verbeeck, J.; Hadermann, J.; van Tendeloo, G. Influence of the Structure on the Properties of $Na_xEu_y(MoO_4)_z$ Red Phosphors. *Chem. Mater.* **2014**, *26*, 3238−3248.
(53) Morozov, V. A.; Bertha, A.; Meert, K. W.; van Rompaey, S.; Batuk, D.; Martinez, G. T.; van Aert, S.; Smet, P. F.; Raskina, M. V.; Poelman, D.; Abakumov, A. M.; Hadermann, J. Incommensurate Modulation and Luminescence in the $CaGd_{2(1-x)}Eu_{2x}(MoO_4)_{4(1-y)}(WO_4)_{4y}$ ($0 \le x \le 1$, $0 \le y \le 1$) Red Phosphors. *Chem. Mater.* **2013**, *25*, 4387−4395.
(54) Becerro, A. I.; Allix, M.; Laguna, M.; González-Mancebo, D.; Genevois, C.; Caballero, A.; Lozano, G.; Núñez, N. O.; Ocaña, M. Revealing the Substitution Mechanism in Eu^{3+}:$CaMoO_4$ and Eu^{3+},Na^+:$CaMoO_4$ Phosphors. *J. Mater. Chem. C* **2018**, *6*, 12830−12840.
(55) Asakura, H.; Hosokawa, S.; Teramura, K.; Tanaka, T. Local Structure and L_1- and L_3-Edge X-Ray Absorption Near Edge Structures of Middle Lanthanoid Elements (Eu, Gd, Tb, and Dy) in Their Complex Oxides. *Inorg. Chem.* **2021**, *60*, 9359−9367.
(56) Tranquilin, R. L.; Lovisa, L. X.; Almeida, C. R. R.; Paskocimas, C. A.; Li, M. S.; Oliveira, M. C.; Gracia, L.; Andres, J.; Longo, E.; Motta, F. V.; Bomio, M. R. D. Understanding the White-Emitting $CaMoO_4$ Co-Doped Eu^{3+}, Tb^{3+}, and Tm^{3+} Phosphor through Experiment and Computation. *J. Phys. Chem. C* **2019**, *123*, 18536−18550.
(57) Binnemans, K. Interpretation of Europium(III) Spectra. *Coord. Chem. Rev.* **2015**, *295*, 1−45.
(58) Eliseeva, S. V.; Bünzli, J. C. G. Lanthanide Luminescence for Functional Materials and Bio-Sciences. *Chem. Soc. Rev.* **2010**, *39*, 189−227.
(59) Lai, J.; Wang, T.; Zhang, H.; Ye, L.; Yan, C.; Gu, W. Modulating the Photoluminescence of Europium Oxide Nanoparticles by Controlling Thermal Decomposition Conditions. *J. Lumin.* **2019**, *214*, No. 116534.
(60) Gomez, G. E.; López, C. A.; Ayscue, R. L.; Knope, K. E.; Torres Deluigi, M. D. R.; Narda, G. E. Strong Photoluminescence and Sensing Performance of Nanosized $Ca_{0.8}Ln_{0.1}Na_{0.1}WO_4$ (Ln = Sm, Eu) Compounds Obtained by the Dry "Top-down" Grinding Method. *Dalton Trans.* **2019**, *48*, 12080−12087.
(61) Razumkova, I. A.; Sedykh, A. E.; Denisenko, Y. G.; Müller-Buschbaum, K. Synthesis and Luminescence Properties of β-$NaRE_{0.95}Eu_{0.05}F_4$ (RE = Y, Lu). *J. Ind. Eng. Chem.* **2020**, *92*, 218−225.
(62) Wang, Z.; Feng, J.; Song, S.; Sun, Z.; Yao, S.; Ge, X.; Pang, M.; Zhang, H. Pure and Intense Orange Upconversion Luminescence of Eu^{3+} from the Sensitization of Yb^{3+}−Mn^{2+} Dimer in $NaY(Lu)F_4$ Nanocrystals. *J. Mater. Chem. C* **2014**, *2*, 9004−9011.
(63) Li, C.; Zhang, C.; Hou, Z.; Wang, L.; Quan, Z.; Lian, H.; Lin, J. β-$NaYF_4$ and β-$NaYF_4$:Eu^{3+} Microstructures: Morphology Control and Tunable Luminescence Properties. *J. Phys. Chem. C* **2009**, *113*, 2332−2339.
(64) Shi, P.; Xia, Z.; Molokeev, M. S.; Atuchin, V. V. Crystal Chemistry and Luminescence Properties of Red-Emitting $CsGd_{1-x}Eu_x(MoO_4)_2$ Solid-Solution Phosphors. *Dalton Trans.* **2014**, *43*, 9669−9676.
(65) Sato, M.; Kim, S. W.; Shimomura, Y.; Hasegawa, T.; Toda, K.; Adachi, G. Rare Earth-Doped Phosphors for White Light-Emitting Diodes. In *Handbook on the Physics and Chemistry of Rare Earths*; Bünzli, J.-C.; Pecharsky, V. K., Eds.; Elsevier, 2016; Vol. *49*; pp 1−128.
(66) Herrmann, A.; Fibikar, S.; Ehrt, D. Time-Resolved Fluorescence Measurements on Eu^{3+}- and Eu^{2+}-Doped Glasses. *J. Non-Cryst. Solids* **2009**, *355*, 2093−2101.

https://doi.org/10.1021/acsanm.3c02136
ACS Appl. Nano Mater. 2023, 6, 15510−15520